4.1 Introduction

Electro-magnetic properties of $SrFe_8Al_4O_{19}$ ferrite can be tailored by either substitution of cations or by different synthesis methods. Studies pertaining to the effect of the synthesis methods over the properties of $SrFe_8Al_4O_{19}$ ferrites are important in understanding their inter relationship which is required to be explored. Properties of $SrFe_8Al_4O_{19}$ materials are strongly altered by the distribution of cations among crystallographic lattice sites which in turn is case sensitive to the synthesis method employed [Kaur and Kaur (2014)]. Selection of the synthesis methods not only depends on the desired properties but also the targeted applications. In this chapter, $SrFe_8Al_4O_{19}$ ferrite has been synthesized by the following three methods, i.e., sol–gel auto combustion, co-precipitation, and solid state method. Optimization of the synthesis method to produce improved electro-magnetic properties for rotating machine applications is also evaluated. Kiani *et al.* (2013) and Safi *et al.* (2016) have reported the synthesis of nanocrystalline magnetic materials by sol-gel auto combustion, co-precipitation and solid state synthesis method. These methods are quick, suitable cost, high simplicity, and nontoxic precursors for industrial scale yielding purpose. Experimental method has been discussed as follows.

To prepare $SrAl_4Fe_8O_{19}$ ferrite by solid state method, Fe_2O_3, $SrCO_3$ and Al_2O_3 are used as raw materials. The stoichiometric composition of raw materials are weighed at Sr : (Fe+Al) = 1 : 12, accordingly. The powders are charged in a zirconia jar. It is subjected to wet ball mill with 1 : 1 mixture solution of DI water and IPA (Iso-propyl alcohol) solution. The ball to raw powder ratio has been kept at 8 : 1 and milled with 400 rpm for 6 hrs. The dried powder is calcined at 1350 °C for 4 hrs to synthesis single phase $SrAl_4Fe_8O_{19}$ ferrite. The calcined powder is granulated with 3 % PVA (poly vinyl alcohol) binder. The granulated

powder further uniaxially pressed at 6 tones/cm^2 to form pellets. The pellets are further sintered at 1390 °C for 2 hrs.

To synthesis $SrAl_4Fe_8O_{19}$ ferrite by co-precipitation method, strontium nitrate [$Sr(NO_3)_2$], aluminium nitrate [$Al(NO_3)_3.9H_2O$] and iron nitrate [$Fe(NO_3)_3.9H_2O$] have been taken in the stoichiometric ratio. The molar ratio of Fe : Sr is maintained at 12 : 1. The solutions of the raw materials are formed with little amount of distilled water. This solution is continuously stirred at 50 °C temperature. NH_3OH solution is being added drop wise to the solution and maintained pH of the solution by 11. NH_3OH solution acts as a precipitating agent in the solution. After maintaining the pH of the solution, the sample is left for 3 hrs for stirring to control the homogeneity of the sample. After 3 hrs, precipitation is washed through distilled water and dried at 100 °C in the oven for 5 hrs. The dried powder is grinded and kept for calcination at 1100 °C for 2 hrs to get the single phase $SrAl_4Fe_8O_{19}$ ferrite. After calcination, 3 % PVA is added into the ground powder. Granulated powder is pressed at 6 tones/cm^2 to form pellets. Formed pellet is sintered at 1250 °C for 2 hrs in an air atmosphere.

The detail methodology of $SrAl_4Fe_8O_{19}$ ferrite via sol-gel auto combustion route has been explained in the experimental chapter (section 3.1.1). The thermal behavior, phase analysis, microstructural and electro-magnetic properties of the ferrites are investigated.

4.2 Results & Discussion

Figure 4.1 shows the TG and DTA curve of the dried gel, obtained from the sol-gel auto combustion process. The thermal decomposition nature of the dried gel has been studied. DTA curve shows three endothermic peaks at 94, 240, and 855 ºC and two exothermic peaks at 190, and 330 ºC, respectively. On the other side, TG shows weight loss

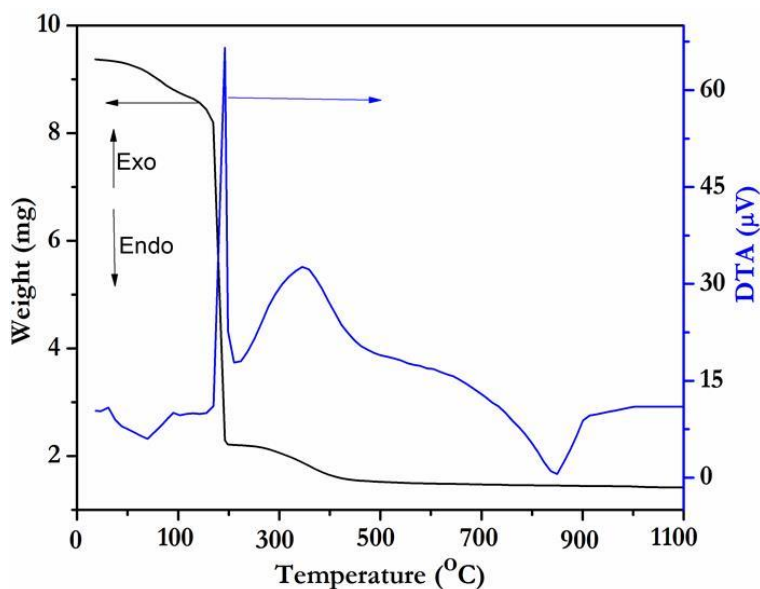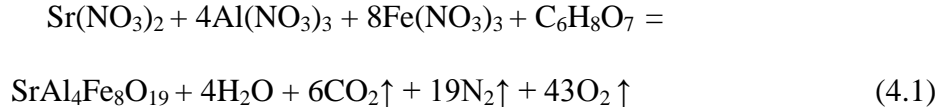in two stages. The first stage appears from 50-110 °C, and second stage weight loss shows from 190 ℃ onwards.

Figure 4.1 TG-DTA graph for $SrAl_4Fe_8O_{19}$ dried gel.

The endothermic peak at 94 ℃ indicates the removal of absorbed water from the dried gel. This dehydration process also produces a TG weight loss in the region of 50-110 °C. While, the DTA peak at 240, and 855 ℃ may be ascribed to the transformation of hydroxides to oxides and formation of strontium ferrite, respectively [Ashiq *et al*. (2011)]. Two exothermic peaks in the DTA curve at 190, and 330 ℃, indicate the autocatalytic anionic oxidation–reduction reaction between the nitrates and citric acid and formation of mono hexaferrite, respectively [Ahmad *et al*. (2012)]. The combustion process is an exothermic process, where, anionic redox reaction occurs between the reductant, i.e., carboxyl group and oxidant, i.e., NO^{-3} ions of the gel [Yue *et al*. (1999), Wu and Huang (2004)]. In the combustion reaction, heat is being induced for supplying the needed energy for reaction between the components to synthesize hexaferrite by solid state diffusion

procedure [Gajbhiye *et al*. (1995)]. Throughout the combustion process H_2O, CO_2, and N_2 gasses are formed. The combustion reaction of $SrAl_4Fe_8O_{19}$ can be understood as:

$$Sr(NO_3)_2 + 4Al(NO_3)_3 + 8Fe(NO_3)_3 + C_6H_8O_7 =$$

$$SrAl_4Fe_8O_{19} + 4H_2O + 6CO_2\uparrow + 19N_2\uparrow + 43O_2\uparrow \qquad (4.1)$$

The sharp weight loss is occurred at 194 ^{o}C. It may be caused by the autocatalytic anionic oxidation-reduction reactions of nitrates and citric acid along with released residual organic matters and nitrates, as shown in equation 4.1. The last peak starts from 855 ^{o}C and gets completed at 1010 ^{o}C due to the formation of strontium hexaferrite. So, the calcination temperature may be selected at 1100 ^{o}C for all the auto combustion synthesized samples.

Figure 4.2 (a) shows the XRD patterns of the sol-gel auto combustion (SG), co-precipitation (CP) and solid state (SS) synthesized calcined powders, which are calcined at 1100 °C for 2 hrs. From the Figure 4.2 (a), it can be seen that all the reflections of 'SG' and 'CP' are belonging to the single phase M-type strontium ferrite (JCPDS No. 720739) [Debnath *et al*. (2015)] with no other secondary phases. The broad reflection peaks of 'CP' sample indicates the poor crystallinity compare to 'SG' sample, which displays the most intense and sharp peaks with higher degree of crystallinity. While in 'SS' sample, pure phase of strontium ferrite is not formed at 1100 °C temperature. The calcination temperature of the 'SS' sample is increased to 1350 °C and it shows single phase, as shown in Figure 4.2 (b). The reflection patterns are well coordinated with M-type strontium ferrite (JCPDS No. 720739) with *P63/mmc* space group [Debnath *et al*. (2015)] and no other secondary phase formation.

To explore more structural parameters, Rietveld refinement is followed out by using the software FullProf with *P63/mmc* space group [Raju *et al*. (2018)]. Rietveld refinement of

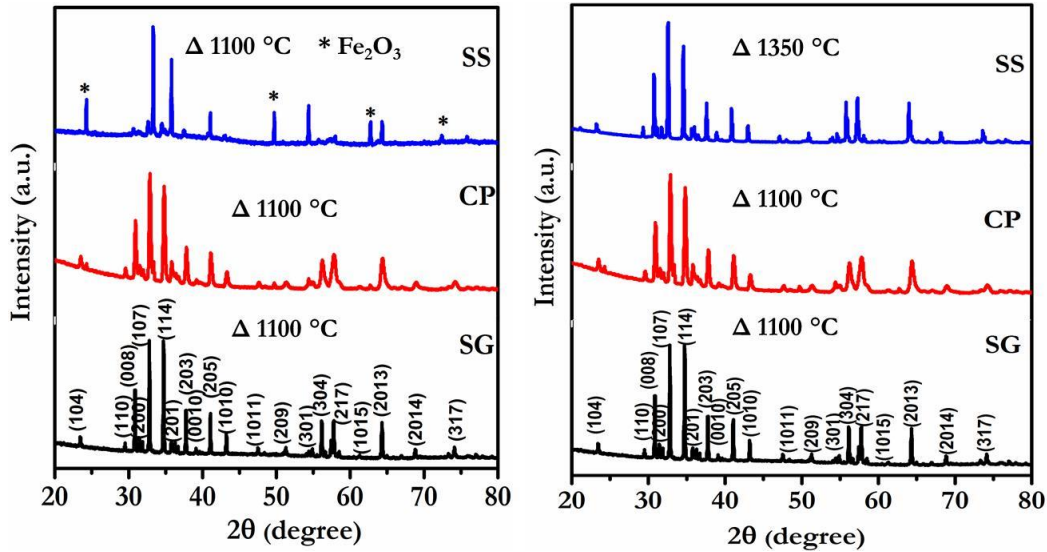the XRD patterns of $SrAl_4Fe_8O_{19}$ ferrite of 'SG', 'CP' and 'SS' are manifested in Figure 4.3.

Figure 4.2 (a) XRD pattern of $SrAl_4Fe_8O_{19}$ powders calcined at 1100 °C temperature with different synthesis routes, (b) XRD pattern of $SrAl_4Fe_8O_{19}$ powders calcined at different temperatures with different synthesis routes.
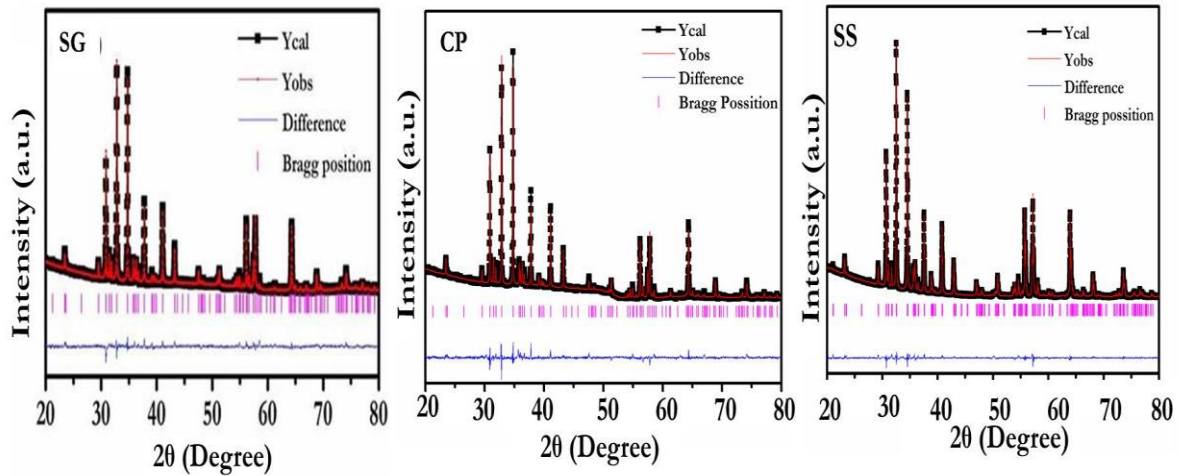

Figure 4.3 Rietveld refined patterns of $SrAl_4Fe_8O_{19}$ ferrite with different synthesis routes.

During the refinement, zero-correction, scale-factor, lattice parameters, thermal parameters, asymmetry parameters, and atomic positions are refined simultaneously.

Background and peak shapes are defined by the linear interpolation among set background points, and pseudo-Voigt function, respectively. The credibility of the refinement is estimated by the low values of R_p, R_{wp}, and χ^2 (goodness of fit). The refined parameters, i.e., reliable factors, lattice parameters, *c/a* ratio, crystallite size, and volume are included in Table 4.1.

Table 4.1 R_p, R_{wp}, χ^2, lattice parameters, *c/a* ratio, crystallite size, and volume of

SrAl$_4$Fe$_8$O$_{19}$ hexa-ferrites.

Different synthesis routes	R_p (%)	R_{wp} (%)	χ^2	Lattice parameters (Å)		c/a	Crystallite size (nm)	Volume (Å^3)
				(a)	*(c)*			
SG	2.06	2.65	1.65	5.78	22.72	3.93	12.64	657.34
CP	3.31	4.29	3.37	5.78	22.81	3.94	30.34	658.99
SS	2.71	2.60	1.98	5.82	22.98	3.94	161.60	673.93

From Table 4.1, the lowest lattice parameters (LP) '*a*' and '*c*' are observed by 'SG' prepared sample, whereas, LP's are increased a bit in 'SS' prepared sample. It illustrates that lattice parameter gets affected by the different synthesis processes. *c/a* ratio is an important factor that validates the M-type structure. For the magnetoplumbite structure, this ratio should be lesser than 3.98. Since the estimated *c/a* parameters in this study are less than 3.98, it confirms the formation of the magnetoplumbite structure in the present matrix [Zhang *et al*. (2012)]. The crystallite size is measured by the Debye Scherrer's formula with using Caglioti equation, as described in section 3.2. It is noted that small crystallite size is obtained by the sol-gel auto combustion method, while bigger crystallite sizes are obtained by the co-

precipitation and solid state preparation method, respectively. Unit cell volume also gets affected by the synthesis method as well. From Table 4.1, maximum volume expansion is observed in 'SS' prepared sample. While, lowest volume is found in 'SG' prepared sample.

Figure 4.4 illustrates the FTIR bands of calcined $SrAl_4Fe_8O_{19}$ ferrite powders with different synthesis processes in the frequency from 4000 to 400 cm^{-1}. Hexaferrite exhibits 189 optical modes, out of them only 31 (13 A_{2u} + 18 E_{1u}) are IR respond modes [Mahadevan *et al*. (2017)]. In the current case, only 3 are active modes 451, 568, and 613 cm^{-1}. Absorption bands between 400 to 800 cm^{-1} are the signature characteristic bands of $SrFe_{12}O_{19}$ [Baykal *et al*. (2012a), (2012b), Xie *et al*. (2012)]. The frequency around 451 cm^{-1} is credited to the intrinsic stretching vibrations at the octahedral site of the metal cation [Gonzalez *et al*. (2017), Mahadevan *et al*. (2017)]. On the other side, absorption frequencies around 568 cm^{-1} and 613 cm^{-1} are due to stretching vibrations of the metal cation at the tetrahedral site [Gonzalez *et al*. (2017), Mahadevan *et al*. (2017)]. In Table 4.2, the vibrational intensities with the different synthesis routes are listed. It can be understood that all the vibration frequencies, which are observed in this range, denotes SrM phase. The nonexistence of the higher frequency band is suggesting the completion of the redox reaction for hexaferrite formation.

Table 4.2 Band position of $SrAl_4Fe_8O_{19}$ ferrite with different synthesis routes.

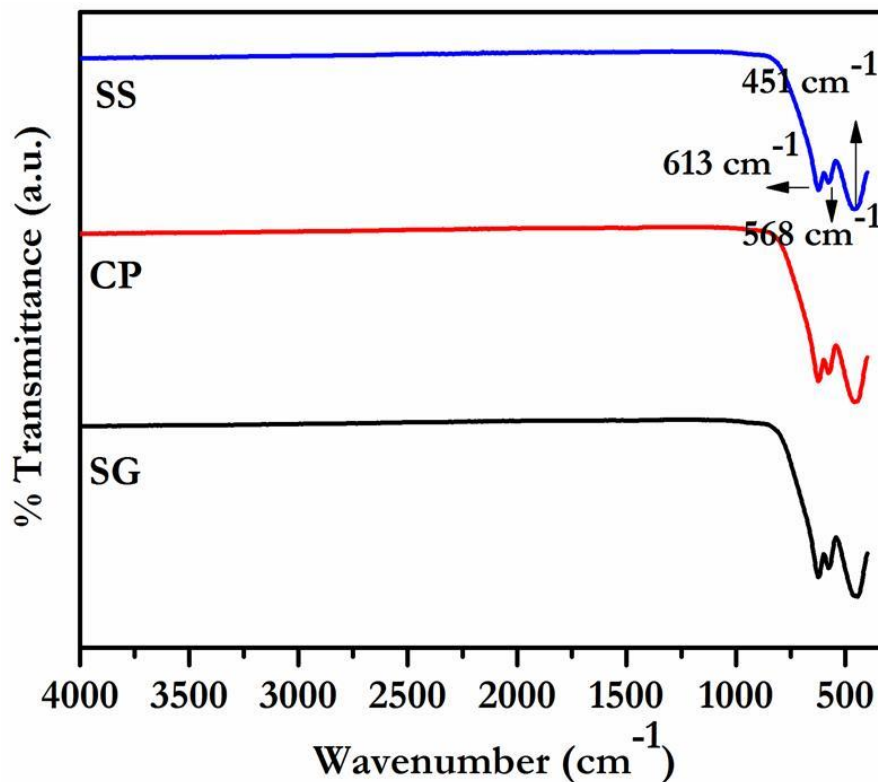| Different synthesis routes	υ_1 (cm^{-1})	υ_2 (cm^{-1})	υ_3 (cm^{-1})
SS	401	568	613
CP	427	570	615
SG	443	574	621

Figure 4.4 FTIR spectra of calcined $SrAl_4Fe_8O_{19}$ ferrite powders with different synthesis routes.

Figure 4.5 shows the morphology of sintered $SrAl_4Fe_8O_{19}$ ferrite samples of 'SG', 'SS', and 'CP'. It shows that all the grains are in well-cleared hexagonal platelet shape with clear boundaries. Grains are elongated in the c-direction [Zhang *et al.* (2016)]. These all lengthened structures also observed by Cespedes *et al.* (2017). It is obligatory for magnetization of strontium hexaferrite [Kim *et al.* (2016)]. Average size of grains are determined by the linear intercept through image J software and enlisted in Table 4.3 along with bulk density. It is noted that 'SG' and 'CP' samples show lower densed narrow sized grains, whereas, 'SS' sample produces highly densed coarse sized grains, as shown in Figure 4.5. EDX elemental analysis is performed to confirm the chemical composition of synthesized $SrAl_4Fe_8O_{19}$ ferrite, as represented in the Figure 4.6.
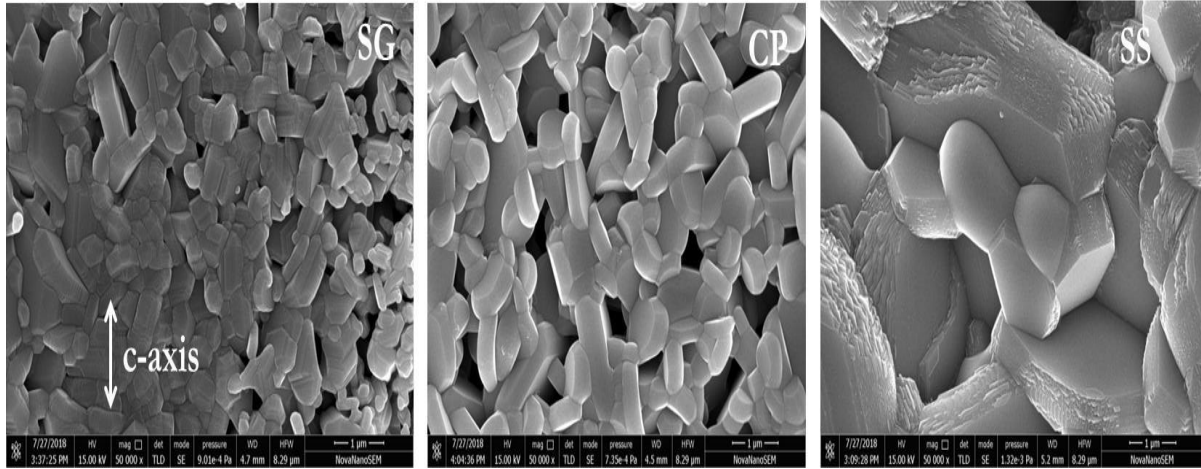
Figure 4.5 SEM micrograph of sintered $SrAl_4Fe_8O_{19}$ ferrite with different synthesis routes.

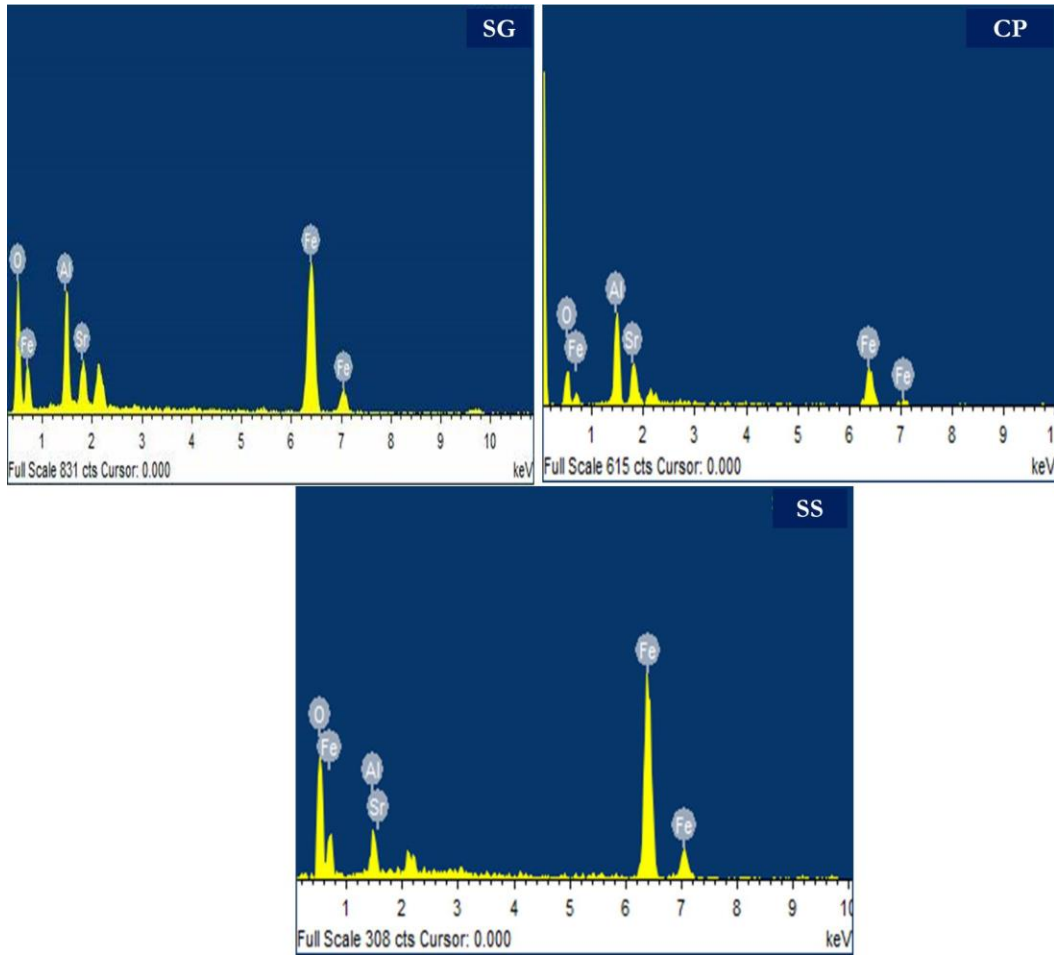**Figure 4.6** EDX micrograph of sintered $SrAl_4Fe_8O_{19}$ ferrite with different synthesis routes.

Table 4.3 Grain size, bulk density and Theoretical density of sintered $SrAl_4Fe_8O_{19}$ ferrite with different synthesis routes.

Different synthesis routes	Grain Size (μm)	Density (g/cm³)	Theoretical density
SG	1.11	5.08	5.10
CP	1.35	5.10	5.12
SS	2.03	5.21	5.25

Figure 4.7 to Figure 4.11 have manifested the magnetic behavior of the sintered samples. Figure 4.7 shows the M–H loops of $SrAl_4Fe_8O_{19}$ hexaferrites with different synthesis methods up to 7 Tesla of an applied field. The alteration of remanent magnetization (Br) with density is shown in Figure 4.8 with a function of synthesis methods.
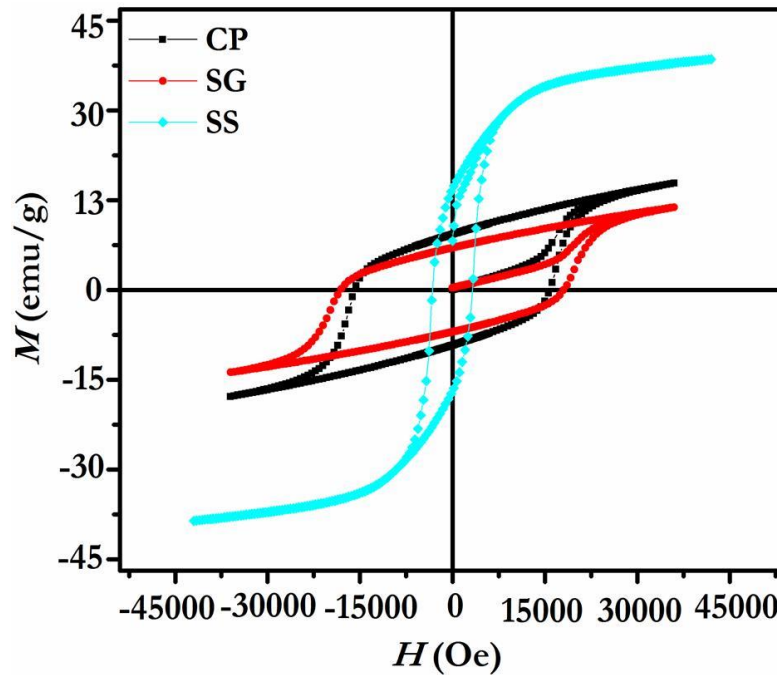

Figure 4.7 Magnetization (M) versus field (H) curves of $SrAl_4Fe_8O_{19}$ hexaferrite with different synthesis methods.
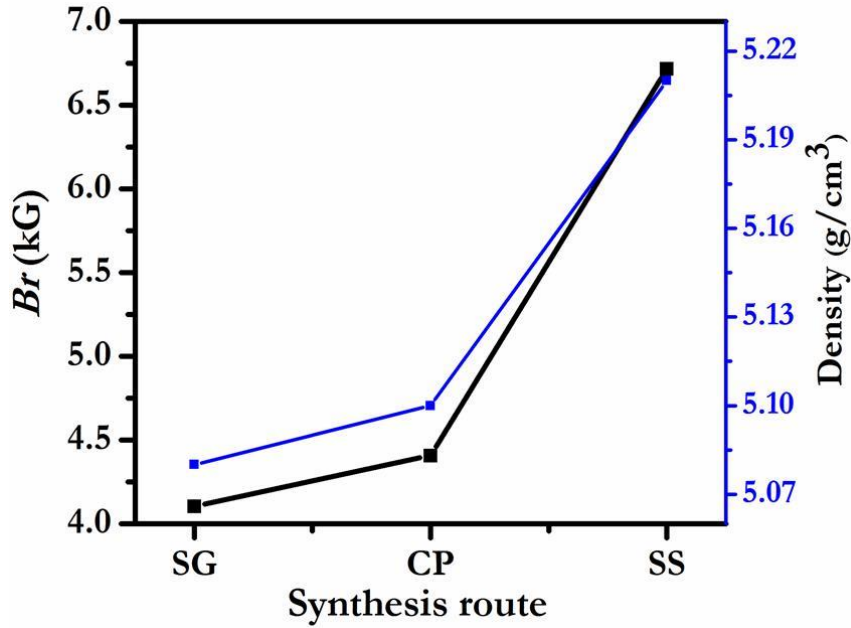
59

Figure 4.8 *Br* and bulk density as a function of synthesis route.

Magnetic properties of SrM are a combination of intrinsic plus extrinsic properties. Intrinsic property, i.e., *Br* mostly depends on the magnetic moment and bulk density [Cui *et al*. (2014)]. Table 4.3 shows the variation of bulk density with synthesis routes. It is observed that synthesis route affects the density of the prepared sample. 'SG' prepared sample shows the lowest density, whereas, density is increased in 'CP' and 'SS' sample, respectively. Increased density enhances the magnetic dipole per unit volume. The magnetic moment (μ_B) is calculated and presented in Table 4.4 along with *Br*, *iH_c*, *bH_c*, k_{eff}, *Mr/Ms*, Squareness ratio (*H_k/iH_c*) and *(BH)_{max}* of $SrAl_4Fe_8O_{19}$ hexa-ferrite with different synthesis routes. It is listed that the large magnetic moment is achieved by 'SS' prepared sample. Density and magnetic moments are responsible factor for enhancement in the magnetization of the system. Hence, *Br* increases in 'SS' prepared sample, while, lower for 'CP' and 'SG' sample, respectively, as shown in Figure 4.8.

Table 4.4 *Br*, μ_B, *iH$_c$*, *bH$_c$*, k$_{eff}$, *Mr/Ms*, Squareness ratio (*H$_k$/iH$_c$*), *and (BH)$_{max}$* of

SrAl$_4$Fe$_8$O$_{19}$ hexaferrite with different synthesis routes.

Different synthesis routes	*Br* (kG)	Bohr magneton (μ_B)	*iH$_c$* (kOe)	*bH$_c$* (kOe)	k$_{eff}$ x10^6 (erg/cm^3)	*M$_r$/M$_s$*	*H$_k$/iH$_c$*	*(BH)$_{max}$* (MGOe)
SG	4.105	4.02	18.15	18.02	3.54	0.482	0.89	6.03
CP	4.407	4.97	16.97	14.10	2.58	0.470	0.88	5.68
SS	6.717	5.48	4.32	4.04	1.13	0.493	0.86	5.03

The variation of *iH$_c$* (intrinsic coercivity) and *bH$_c$* (magnetic induction coercivity) with synthesis routes have been shown in Figure 4.9. The *bH$_c$* (magnetic induction coercivity) is the magnetic field which causes the induction (*B*) allocation in the magnet to alter its direction. It is normally lesser than *iH$_c$* (intrinsic coercivity). From Figure 4.9, it is detected that the maximum coercivity *(iH$_c$* and *bH$_c$)* is observed for sol-gel auto combustion process, i.e., 'SG'. This behavior is dependent on the magneto-crystalline anisotropy and grain size of the system [Singhal *et al*. (2010), Almessiere *et al*. (2018)]. Magneto-crystalline anisotropy constant (k$_{eff}$) of the system is calculated by the law of approach method of Stroner-Wohlfarth (S-W) model [as discussed in the section 3.5] for these methods, as shown in Figure 4.10, respectively. With synthesis method, k$_{eff}$ value is varied and observed maximum k$_{eff}$ for sol-gel auto combustion method. The increment in *iH$_c$* is due to the decrease in the size of grains. The increment of grains is responsible for decreasing the grain boundaries that contribute to the obstruction of domain wall motion, thus decreasing the coercivity [Hooda *et al*. (2015)].
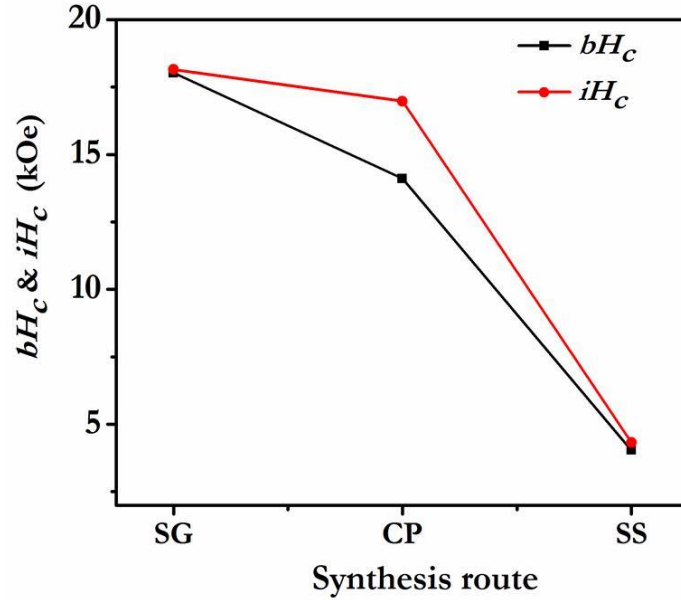
Figure 4.9. Magnetic induction coercivity (bH_c) and intrinsic coercivity (iH_c) of SrAl$_4$Fe$_8$O$_{19}$
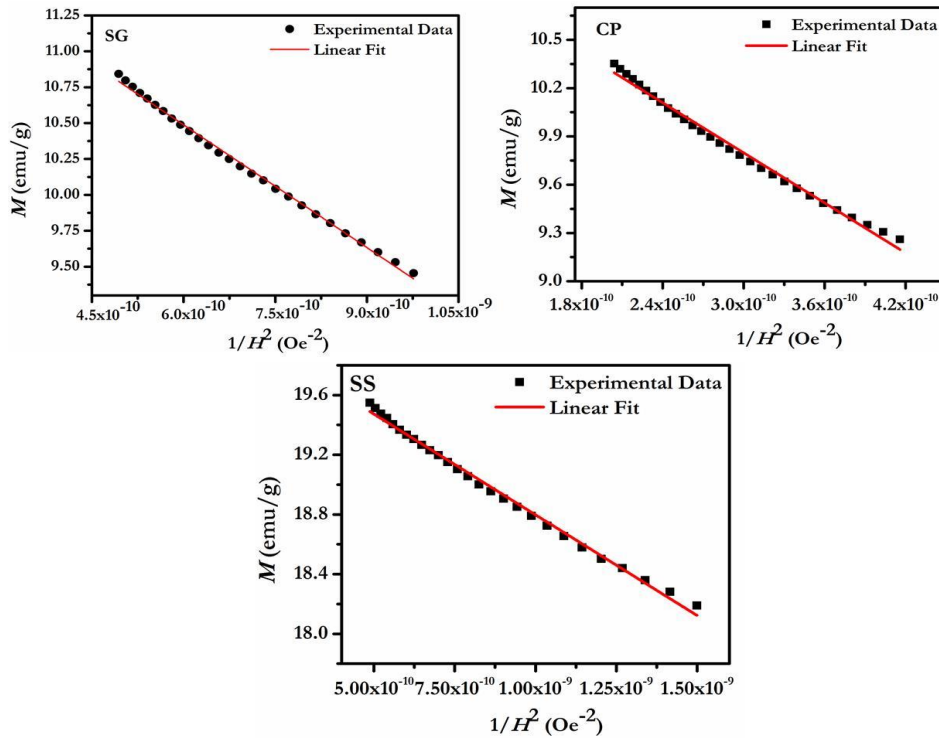
hexaferrite with different synthesis methods.

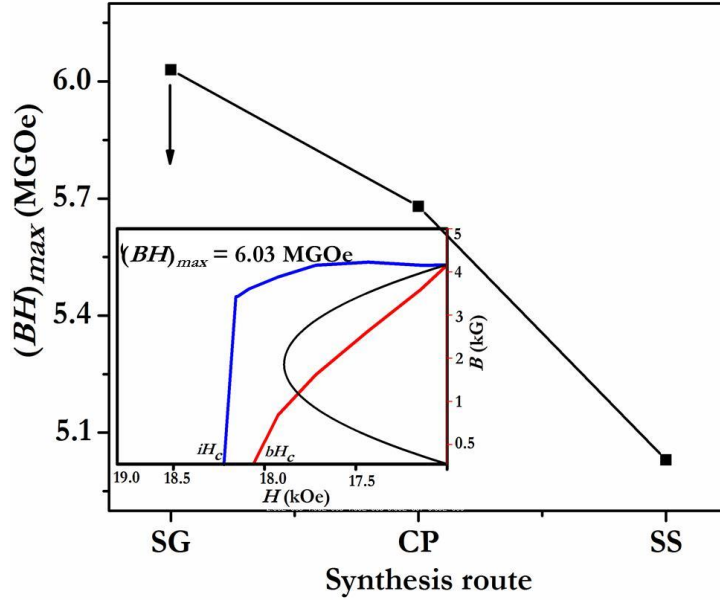**Figure 4.10** Magnetization versus $1/H^2$ plots for SrAl$_4$Fe$_8$O$_{19}$ ferrite with different synthesis

methods.

Figure 4.11 *(BH)$_{max}$* of the prepared SrAl$_4$Fe$_8$O$_{19}$ ferrite as a function of the synthesis methods.

It has been stated that if the material is in single domain region (M_r/M_s ratio >0.5), as the grain size decreases then coercivity decreases due to thermal effect and iH_c is expressed as, $iH_c = g - q/s^2$, where, g and q are constants in single domain structure. In the multi-domain region (M_r/M_s ratio <0.5), coercivity decreases when, the grain size increases [Verma *et al*. (2016)]. It seems to be associated with the surface area and iH_c can be articulated as $iH_c = e + f/s$, where, 'e' and 'f' are constants and 's' is the diameter of the particle in the multi domain region. These compositions show multi domain nature in the matrix. Bigger the grain sizes, smaller will be the grain boundaries. Grain boundaries perform as pinning sites for the domain wall movement and it leads to restricting the rotation of magnetization [Thakur *et al*. (2013b)]. Therefore, decreasing the coercivity with the increasing in grain size.

Table 4.4 shows the ratio of H_k/iH_c, i.e., squarness ratio of hexaferrite. H_k is the knee field which affects anisotropy factor (α). It specifies the oblongness of the demagnetization

graph for the ferrites. It is observed that the squarness ratio is decreased from 'SG' to 'CP' and 'SS' sample. It is varied with the variation of coercivity of the sample. Generallly, if the values of the H_k/iH_c ratio is >0.85, usually it is considered for square loop ferrite, i.e., permanent magnet. Figure 4.11 shows the energy product $(BH)_{max}$ with the function of synthesis routes. Maximum $(BH)_{max}$ is observed for 'SG' prepared sample and decreased for 'CP' and 'SS' prepared sample. The maximum value 6.03 MGOe is achieved for 'SG', as displayed in Figure 4.11.

Figure 4.12 shows the dielectric constant (ε) variation with frequency and Table 4.5 summarizes the values at 1 MHz along with resistivity (ρ) of sintered $SrAl_4Fe_8O_{19}$ ferrite with different synthesis routes. The ε of the synthesized sample is calculated by the equation 3.16. It is cleared from the Figure 4.12 that dielectric constant is decreased with frequency. According to Iwauchi (1983), the dielectric polarization mechanism is due to the electrons hopping in ferrites alike to the conduction mechanism.
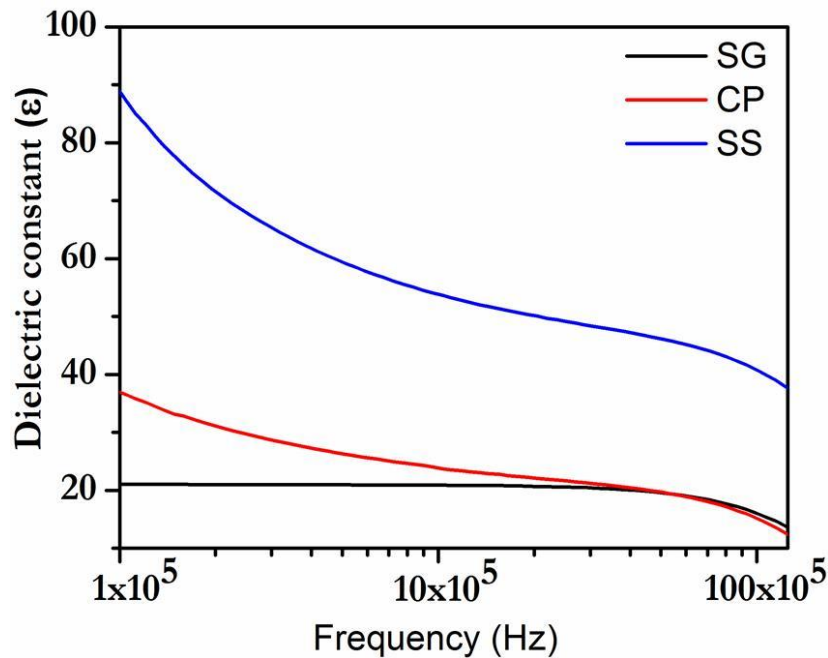

Figure 4.12 Dielectric constant as a function of frequency with different synthesis methods.

When the electric field is functional to the dielectric, space charge (SC) polarization is occurred due to the electron displacement. The SC polarization depends upon the electron exchange among Fe^{+2} and Fe^{+3} ions. At low frequency, it contains large dielectric constant may be because of hopping of the electrons, which may easily follow the applied field and results large polarization. While at high frequency, the hopping of the charge may not track the applied field. In dielectric, space charge carriers take fixed time to track up their axes corresponding to the ac field. If the frequency of the applied field increases reversely then, SC carriers cannot maintain with the field and the alternation of their direction falls back of the field [Ajmal *et al*. (2010)]. Hence, the net dielectric constant decreases at high frequency. From Table 4.5, it is found that ε is increased from 'SG', 'CP' to 'SS' sample. This variation in ε is observed due to the variation in the grain size. Maximum grain size is found in 'SS' synthesized sample and it is decreased with 'CP' and 'SG' prepared sample. Due to increment in the grain size, ion polarization may be increased with the growth of grain necking. The ions polarizations greatly affect the dielectric constant [Hassan *et al*. (2014)]. When, the grain size is increased, it decreases the grain boundary concentration among them. As a result, it reduces the limitation in the motion of the domain wall, which improves the dielectric constant.

Figure 4.13 shows the changes in AC resistivity (ρ) with frequency. All samples demonstrate a decrease in ρ with the rise in frequency. It is observed that resistivity increases with 'SS', 'CP' and 'SG' prepared sample. Nature of resistivity can be defined based on grain size. As listed in Table 4.3, the grain size is decreased for sol-gel auto combustion method. Decreasing in grain size, enhances the grain boundary (GB) area. Grain boundary

obstructs the electron transfer, therefore, highest resistivity is observed for 'SG' sample and decreases with followed up by 'CP and 'SS' prepared sample.

Table 4.5 Dielectric constant ($\mathcal{E}$) and resistivity (ρ) of sintered $SrAl_4Fe_8O_{19}$ ferrite with

different synthesis routes.

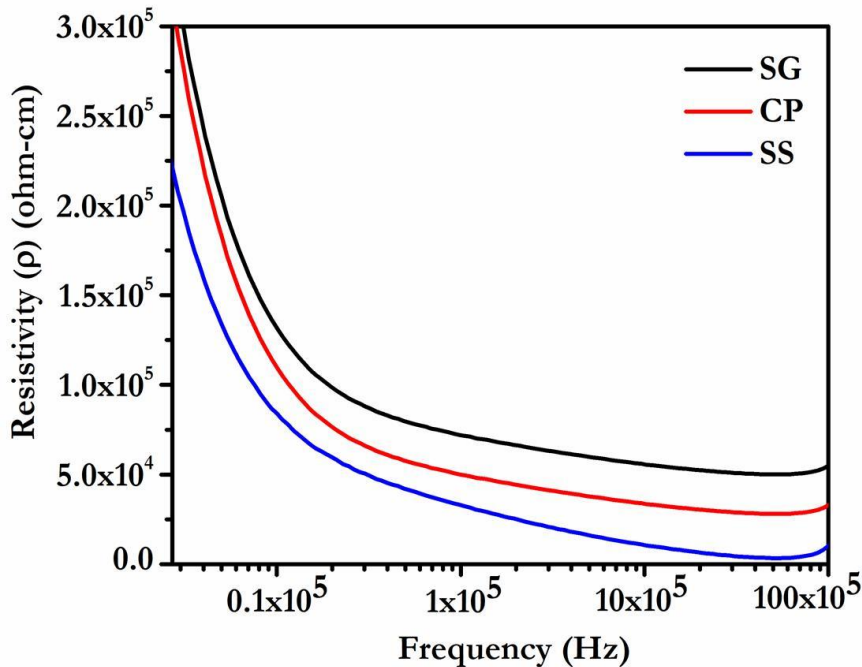| Different synthesis routes	$\mathcal{E}$ at 1MHz	ρ (Ω-cm)*10^4 at 1MHz, 298K
SG	20.52	5.54
CP	23.67	3.34
SS	53.67	1.04

Figure 4.13 Resistivity as a function of frequency with different synthesis methods.

4.3 Summary

$SrAl_4Fe_8O_{19}$ hexaferrites are synthesized by the solid state, co-precipitation and sol-gel auto combustion process. Solid state method confirms that high calcination temperature is

required to synthesis pure strontium hexaferrite phase. While, sol-gel auto combustion route forms single phase of strontium hexaferrite with high crystallinity. Rietveld refinement exposes that all the samples have hexagonal crystal symmetry with *P63/mmc* space group. SEM micrograph shows hexagonal pelletlet shapes in all the samples. Variation is observed in crystallinity, bulk density, grain size, magnetic parameters like *Br*, *iH$_c$*, *bH$_c$*, *(BH)$_{max}$* and dielectric constant in the prepared $SrAl_4Fe_8O_{19}$ ferrite due to different synthesis processes. Improved intrinsic coercivity (*iH$_c$*) is observed in sol-gel auto combustion process due to smaller grain size formation and large k$_{eff}$. Sol-gel auto combustion process achieves maximum *(BH)$_{max}$* up to 6.03 MGOe compare to co-precipitation and solid state process. Thus, the nominal sol-gel auto combustion method is optimized to synthesis the further substituted $SrAl_4Fe_8O_{19}$ ferrites in the next sections. In the next following sections, the influence of non-rare earth ions (Co^{+2} and Cr^{+3}/Sn^{+4}) and rare earth ions (Y^{+3} and La^{+3}/Sm^{+3}) substituted $SrAl_4Fe_8O_{19}$ ferrites, prepared by sol-gel auto combustion route, will be investigated.